Title: Bowtie design for thermal expansion mimicry and mitigation

Abbreviated Title: Bowtie design

Author: Jimmie Miller (corresponding author, jamiller@charlotte.edu)

Affiliation: Center for Precision Metrology, W. S. Lee College of Engineering, The University of North Carolina at Charlotte

9201 University City Blvd, Charlotte, NC 28223

Abstract

A geometric bowtie design for the purpose of mimicking (matching) and/or mitigating (reducing) the thermal expansion effects between two laterally placed structures is investigated. A bowtie design is that of two opposing overlapping triangles with farthest sides parallel. This design embodies thermal centering concepts which utilize the relationships of the trigonometric identity known as the law of sines for a triangle from which beneficial thermal properties can be engineered. For validation. The bowtie design is embodied using two separated Zerodur plane mirrors, symmetrically opposed, and each seated in Maxwell-style kinematic couplings of spheres and vee-groves. The vee-grooves form a wheel-like pattern on an aluminum baseplate. The intersection of the vee-grooves is the common overlapping thermal center of both mirror mounts. The refractive-index corrected interferometric measurement of the displacement between these two mirrors shows that even during non-isothermal non-equilibrium transitions and states, the nominal ~ 90 μm thermally induced (13 ^{0}C) expansion of an aluminum baseplate can be mitigated, being reduced more than 98%

to ~1.4 μm by mimicking the thermal expansion properties of the mirrors' structural material. Engineering thermally-invariant kinematic bowtie designs using materials having higher thermal expansion coefficients is also described.

Key words: thermal expansion, mitigation, kinematic mount/coupling/constraint, bowtie design, thermal center, thermo-symmetric, thermal mimicry

1. Introduction

As is stressed by Slocum: "Errors caused by thermal expansion are among the largest, most overlooked, and misunderstood form of error in the world of machine design" [1]. The same holds true for dimensional metrology setups. Recently (2023) in precision measurement of the Gravitational Constant, G, thermal issues were found to significantly influence the uncertainty of reported values [2]. Also recently, in an article on cloud-based techniques with federated learning, Stoop [3] commented that "Thermal error compensation is one of the most research-oriented topics in manufacturing with rising importance in the industry." Another current area of thermal research is self-optimization with Möhring stating that "one key example … the compensation of thermal error effects that lead to structural deformations, path deviations and inaccuracy … strategies can be passive, such as by thermo-symmetric machine design, or active, … via the NC control or by active temperature control of components." [4].

Furthermore, the measurement and compensation of thermal errors has a long continuing history among instrument and machine designers and users. Accommodating the thermally changing pendulum length and thus time variation, the mercury compensated pendulum clock was introduced by Graham in 1721 and soon followed by Harrison with the gridiron pendulum in 1726 [5]. Bryan [6] attributes to Grand as the first person to explain, in the 1950's, the exact way in which temperature variation affects linear measurements. Schmitt [7] commented that "thermal influences have a great impact on the measurement uncertainty … they typically result in time-varying errors, which require dynamic compensation…. **the significance** … for the dimensional measurement of large-scale components **can be very harsh**."

Referencing the recommendations of a previous work [8], Bryan [6] suggested that future machines be designed for thermal balance considering both the workpieces and frames. Reviewing the current status of thermal error research, Mayr [9] recounted the techniques for compensating and mitigating the thermal issues including compensatory materials, direct measurement and compensation, and also thermal control of ambient and structural coolants, concluding that "More precise measurement devices and measurement strategies should be developed to reduce the uncertainties of temperature and displacement measurement of machine tools and workpieces." The paper self-identified as an update and not substitution of the previous works in which Bryan [10] stated that "thermal effects are still the largest single source of dimensional errors and apparent non-repeatability of equipment."

and Weck [11] relates the difficulty of precise prediction of thermal behavior related to inaccurate knowledge of heat sources, thermal boundary conditions, mechanisms etc. Additionally, due to thermal gradients, systems with linear aerostatic and hydrostatic bearings, as Noste [12] elucidates, "can never be considered at steady state, at least during and for some period after slideway motion". Since steady state operation is elusive with every component in a system having its own time constant, measurement and related corrections become exceeding difficult with increasing uncertainty, thermal errors need to be mitigated in the design and construction before any correction is attempted.

Along with other uses (e.g. thermal stress relief [13] hot gas embossing [14], and Abbe compliant encoder mounting [15]), two-body kinematic couplings have been utilized to limit thermal drift [16] [17] [18] [19] [20] [21] [22] [23] in various instruments for measuring from the atomic scale [24] to the stellar scale [25] [26]. Examples include the x-ray mirror system for the Sirius synchrotron source [27], and the Laser Interferometer Space Antenna (LISA) [28].

. "By mounting components in a kinematic way and by correctly choosing the directions of the constraints, two components can be made thermally invariant at one point, which is called the thermal centre". [29], also defined in [17] and [30]. In this context the two components comprise a single kinematic mount. The novel methodology described in this paper is a passive design utilizing two spatially separated kinematic mounts having common-thermal-centers (TCs) and utilizing the

trigonometric law of sines. The thermal centers are chosen to be substantially external to the physical material of the mount super-structures (i.e. not the base).

The capability of this current embodiment to mitigate by more than 98% the thermal expansion between two physically separated (237 mm) parallel planar mirrors mounted (305 mm separation) on an aluminum plate is described herein and shown graphically in Section 4.

2. Trigonometric Bowtie Principle

The applied trigonometric principle is given and illustrated in Figure 1, where the triangle abc is formed by vertices a, b, and c having α, β, and γ as the interior angles with A, B, and C being the lengths of the sides opposite those angles.

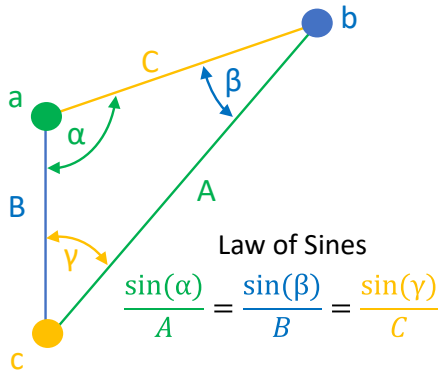

Figure 1. Trigonometric law of sines illustrated.

For this work, a dual symmetric triangle configuration was utilized having a common vertex with opposing sides held parallel thereby producing a bowtie configuration as is shown in Figure 2 . The symmetry is not necessary but convenient. If the lengths of B

and B’ are held constant by material properties along with the angles by mechanical construction, then all the other sides mimic B and B’ material properties maintaining the distance constant from side B to side B’ also.

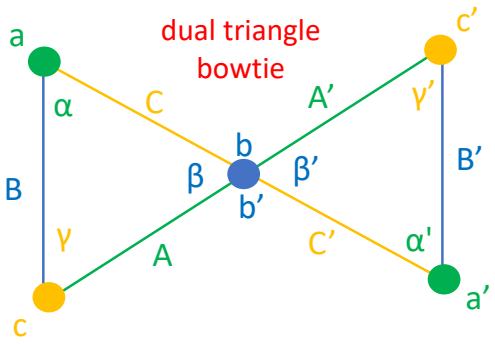

Figure 2. Bowtie configuration utilizing symmetric triangles and the law of sines

3. Physical realization

In order to maintain the angles β and β’ constant, a plate was machined with radially patterned, angled-wall, slots (vee-style grooves) with flat bottoms to seat 1.5” stainless steel balls for gravity-closed [31] kinematic nesting [22]. In thermal equilibrium or slowly varying thermal conditions the vee grooves maintain their planar angular orientation with respect to one another. The plate is shown in Figure 3. The plate was built to accommodate much larger mirrors as a reference for anticipated 2D future projects to assess the mounting and metrology of large freeform

optics (e.g. multi-segmented), tight-tolerance precision manufacturing, refractometry, and dilatometry.

Sides B and B’ are realized by Zerodur mirrors, each kinematically constrained by three steel balls which maintain the α, α’, γ and γ’ angles. Careful construction/alignment also set the mirrors to be nearly parallel [32] to each other so that the perpendicular distance between them is the same at any point. This also facilitates a plane mirror interferometer configuration to measure their thermally induced relative displacement. This is shown in Figure 3. The placement of the interferometer optics near the center is also shown. Also visible are wires to thermistors used for sensing the temperatures of components. Some of the thermistors are not visible due to the mounting putty which holds them in place and thermally isolates them to the structures which they are measuring. Four thermistors are attached to the non-structural simply-supported dark carbon fiber rod (arrow shaft) lying across the mirrors to determine the temperature of the air near the interferometric measurement’s laser path.

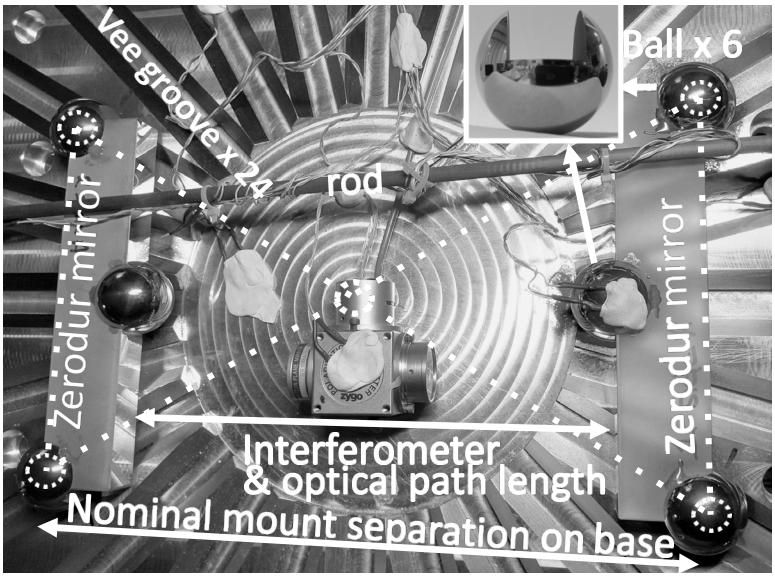

Figure 3. The physically realized bowtie (dashed lines) configuration photographed from above. Each mirror is held by three balls. The balls are kinematically seated in the radially machined vee-groves of an aluminum plate. The outer balls set the vertices of the nearly symmetric triangles. The inset shows electro-discharge machined slot in mounting ball. The apparent distortion is caused by the camera pose.

Mounting balls were electro-discharge machined with a slot to fit around the Zerodur mirror elements to attach (via pressed cyanoacrylate) as near the center of the balls as possible (low tens of micrometers) to prevent the thermal expansion of the balls from significantly affecting the measurements. See inset of Figure 3. The kinematic contact points are below the slots. The thermal center is driven by the intersection of the groove angles on the baseplate. The position of third mounting ball (not one of the bowtie vertices) provides the angular alignment constraints for the mirrors. For the situation demonstrated, the attachment of this ball could have been done with material such as aluminum that has a much large coefficient of thermal expansion than the Zerodur. as long as that expansion does not rotate the mirror portion of the

kinematic mount. This is possible as long as the thermal expansion of the third ball is only in the direction that is outward from the thermal center.

The isolated thermal chamber and system used to facilitate the temperature variation are more thoroughly described in [32]. However, some details will be presented here for completeness. The baseplate was situated via thermally-isolated mounts on a sturdy steel table with T-slots. The table rested on three points using rubber backed-carpet for vibration reduction. There were three two-inch hollow cubes on the table affixed with hot glue for stability. Around these and covering the table top was one inch of foil-faced foam insulation. On top of the cubes was a thin acrylic plate. On top of the thin acrylic plates were glass lenses which provided an XYθ compliant kinematic seat having gravity-fed restoring forces when rocked from equilibrium due to the oblate shape of the lenses. There were three thin acrylic pads on the bottom of the baseplate which were attached with cyanoacrylate. The three pads on the baseplate rested on the lenses completing the mount. There was a resistively heated pet blanket under the baseplate. The blanket was plugged into a alternating current (AC) controller with thermistor feedback capable of ramping and holding the temperature to preselected values. The effect of the ramping can be seen in Figure 4 which shows the measured temperature of the top of the aluminum plate as the control ramped the temperature in three steps both up and down.

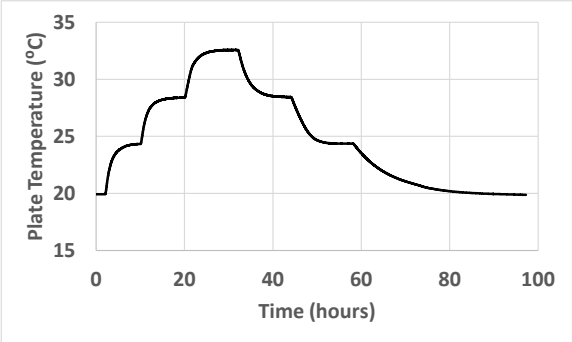

Figure 4. Temperature of the top surface of the aluminum baseplate over time. There were three controlled steps in temperature up and down with differing step durations accounting for the different time constants for heating and cooling.

The times of the ramp-up steps were shorter than the times of the ramp-down steps to assure equilibrium conditions during the ramp down. The cooling time constant of the system was about 6 hours. The controller used an in-built auto-tune algorithm to reduce thermal swings at the equilibrium setpoints. There were a dozen calibrated thermistors (+/- 0.02 ^{0}C) which measured the temperatures of the ambient and various surface points of the baseplate along with the temperatures of the measuring optics and the mounting balls.

4. Interferometric measurement

The setup of the interferometer and beam paths are shown schematically in Figure 5. Measurement is obtained by an Agilent 5529A (now Keysight) laser system. The resolution of measurement is nominally 10 nm but reduced to 5 nm by the double mirror reflection style interferometer which also simplifies its' alignment. That is, the

indications were divided by two before subsequent analysis and graphing in Figure 6 and all other plots.

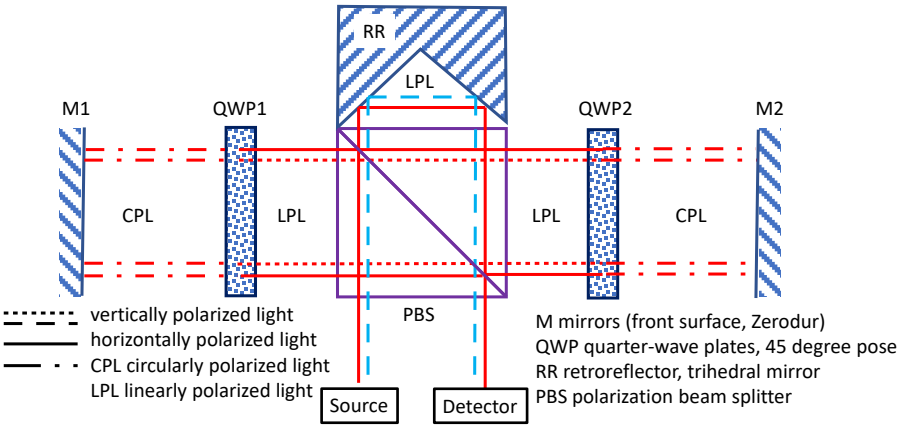

Figure 5. Schematic of the components and beam paths for the mirrors' displacement measurements. The components, beam paths and polarizations are identified. The paths in the PBS optical element are unbalanced. The actual paths setup is over/under and not side-to-side.

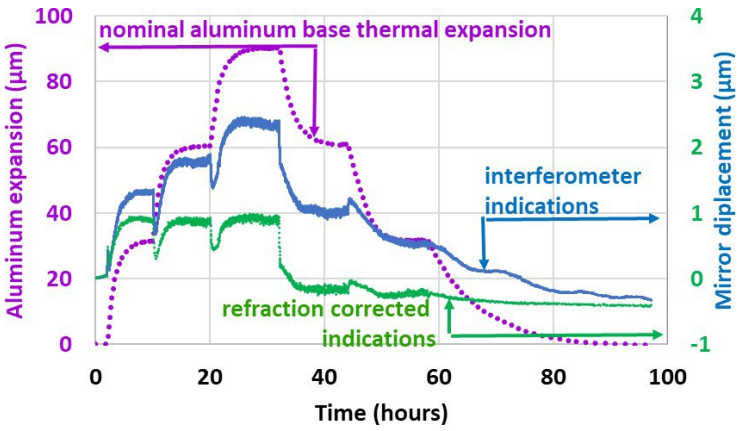

Figure 6. Nominal and interferometric indications between mirrors mounted on an aluminum plate in response to a stepped thermal environment, are plotted. The left axis indicates the base expansion and the right axis the interferometric indications before and after correction for wavelength refraction factors explained in the text.

The laser is a polarization encoded heterodyne source. The polarization beam splitter (PBS) allows one polarization state to pass through to be reflected by a cube corner retroreflector (RR), back through the PBS into the optical pickup optics in the laser head. The PBS reflects the alternate polarization state through a quarter-wave plate (QWP1), reflecting off a mirror (M1), back through QWP1, at which point it's polarization state has rotated 90 degrees, straight through the PBS, on through QWP2, reflecting off M2, back through QWP2 with rotated polarization to be reflected as it passes through the PBS onto the RR and completely re-traverses (below) its original path to exit into the optical pickup optics of the laser head. The difference in path lengths between the original polarization states in nominally equivalent to the change in separation distance between mirrors M1 and M2. Because the paths for the two different polarization states travel a substantial distance difference, the unbalanced portion must be corrected for atmospheric and thermally-related material changes in refractive index and thus the wavelength of light. The observed displacements after corrections as a function of temperature are plotted in Figure 6 and are discussed in a following section.

5. Interferometric index corrections

The unbalanced beam path contains the material between the two mirrors. This consists of path actually in air, l_{air}, the path distance d_{qwp} through the quarter-wave plates, and the path distance d_{pbs} through the polarization beam splitter. The laser system is wavelength corrected to a temperature of 20 ^{0}C and 760 torr of pressure. Subsequent to measurement readings ($m.r$), near nominal corrections for the air path

index variation were made for temperature, pressure, and humidity based on the approximation equation (1) from the informational appendices of the ASME B5.57-1998 standard [33].

$$\Delta_{air} = l_{air}\left[k_T(T_{ai} - 20\ ^0C) - k_p(P_{ai} - 760\ torr) + k_h(V_{ai} - 10\ torr)\right] \quad (1)$$

Where Δ_{air} is the interferometric correction for the ambient variations, l_{air} = 187 mm is the nominal path length in air, k_T = 0.93 x 10-6/^{0}C, k_p = 0.36 x 10-6/torr, k_h = 0.05 x 10-6/torr the constants for correction, and T_{ai}, P_{ai} and V_{ai} being the ambient air's temperature, pressure, and partial pressure of water. The correction for air temperature Δ_{dTi} from experimental start to indication i with T_{ao} the initial air temperature is given by equation (2).

$$\Delta_{dTi} = l_{air}\ k_T(T_{ai} - T_{ao}) = l_{air}\ k_T\Delta_T \quad (2)$$

The pressure displacement correction Δ_{dpi} with P_{ao} the initial air pressure is given by equation (3).

$$\Delta_{dpi} = -l_{air}\ k_p(P_{ai} - P_{ao}) = -l_{air}\ k_p\Delta_p \quad (3)$$

The humidity displacement correction Δ_{dhi} with V_{ao} the initial partial pressure of water vapor in the air is given by equation (4).

$$\Delta_{dhi} = l_{air}\ k_h(V_{ai} - V_{ao}) = l_{air}\ k_h\ \Delta_v$$

(4)

These corrections and their combined effect $\Delta_{air} = \Delta_{dTi} + \Delta_{dpi} + \Delta_{dhi}$ are shown in Figure 7 .

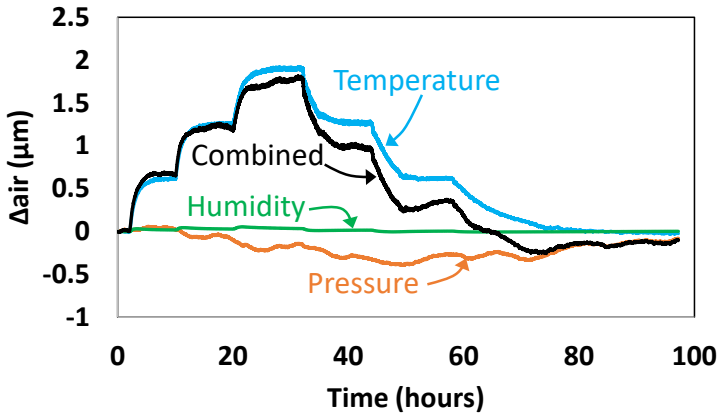

Figure 7. Corrections to the measurements for the changing index of refraction of air due to temperature, humidity, and pressure.

In addition to these corrections it is also necessary to correct for the changing index within the optical elements [34] and the expansion of the optics as their temperature changes. The temperature T_{op} of the PBS, QWP1 and QWP2 was estimated by measuring the temperature at the top of the outer housing of the interferometer. These elements were made of BK7 glass and its properties [34] [35] were used to do the correction calculations. The optical elements had a total nominal unbalanced path length $l_{op} = d_{qwp} + d_{pbs}$ = 50.8 mm. Equation (5) shows the correction for the optics expansion $\Delta_{exp.op}$.

$$\Delta_{exp.op} = l_{op}\,\alpha_{BK7}\Delta T_{op}(n_{BK7} - n_{air})$$

$$\approx l_{op}\alpha_{BK7}\Delta T_{op}(1.51509 - 1.00027) = D_{\alpha.op}\Delta T_{op} = l_{op}k_{\alpha.op}\Delta T_{op}$$

(5)

The value [35] for BK7 glass (α_{BK7}) is 7.1e-6/K and ΔT_{op} is the measured deviation from 20 ^{0}C. $D_{\alpha.op}$=183 nm/K and $k_{\alpha.op}$ = 3.16 μ/K for the configuration described. The change in the index of refraction of the optics was calculated through equation (6) after [34] .

$$\Delta_{n.op} = \frac{n^2(T_o) - 1}{2\, n(T_o)} \left(D_0 \Delta T_{op} + D_1 \Delta T_{op}^2 + D_2 \Delta T_{op}^3 + \frac{E_0 \Delta T_{op} + E_1 \Delta T_{op}^2}{\lambda^2 - \lambda_{TK}^2} \right)$$

(6)

The values used [35] for a 632.8 nm wavelength are n=1.51509, λ= 0.6328 μm, D_0=1.86e-6/K, D_1=1.31e-8/K^2, D_2=-1.37e-11/K^3, E_0=4.34e-7 (μm)^2/K, E_1=6.27e-10 (μm)^2/K^2, and λ_{TK}=0.17 μm. This equation was quite linear for the range of temperatures effected so that the optical path distance can be determined using equation (7).

$$\Delta_{opl.n.op} = l_{op} \Delta_{n.op} \approx D_{n.op} \Delta T_{op} = l_{op} k_{n.op} \Delta T_{op}$$

(7)

The linear fit of $\Delta_{n.op}$ vs ΔT_{op} provided the slope $D_{n.op}$ = 68.5 nm/K with an R^2>0.995 over the range of interest. This also yields a constant to be used in calculating the uncertainty $k_{n.op}$=1.18 μ/K. The compensation values Δ_{op} = -$\Delta_{opl.n.op}$ - $\Delta_{exp.op}$ for the total index of refraction considerations are shown in Figure 8 .

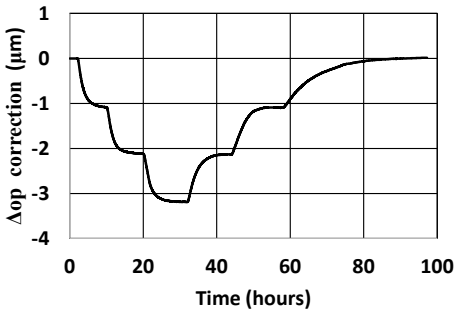

Figure 8, The corrections made for the thermally changing index of refraction affecting the optical path length through the interferometer optics.

The described corrections were made to the mirror displacement laser readings $\Delta_{m.r}$ to obtain the corrected mirror displacements $\Delta_{m.c}$ with the results shown in Figure 9. While the displacements are small, there are still features of significance. These features are identified by dotted and dashed ovals in Figure 9. Whitehead [36] states that there are two classes of errors: "those that only have to be recognized in order that they may be effectively eliminated and; and those errors that determine the accuracy…." Since the features are recognizable it may be possible to identify the sources and skillfully eliminate them.

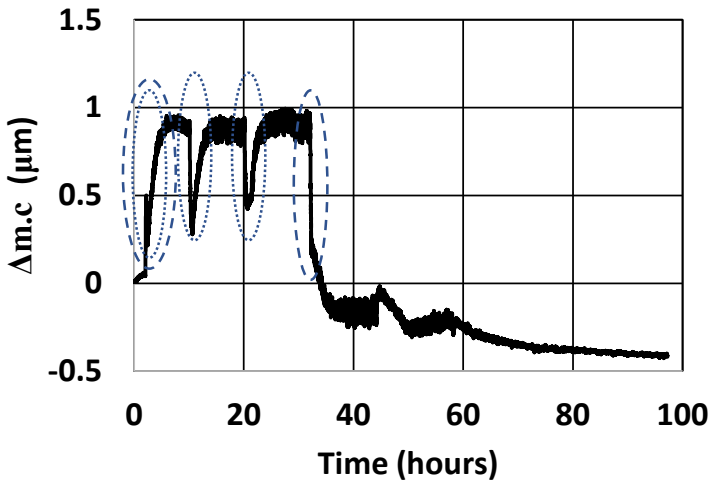

Figure 9. Displacement between mirrors after correction for the changing index of air and optics. The circled regions are thermal non-equilibrium regions of interest described further in the text.

The two regions indicated by dashed ovals appear to be a hysteretic effect that is dependent on the direction of the temperature change with an increase in temperature effecting an increase in apparent mirror separation. The dotted oval enclosed regions happen when there is a larger temporal slope for the temperature swing and temporarily decrease the separation with positive thermal swing.

Identified possible sources for these effects include ball/Zerodur adhesive joint compliance actuated by the sliding friction of the ball/aluminum kinematic interface, structural bowing of the plate due to non-equilibrium dynamic thermal states, changing water layer thickness on the mirror surfaces [37] and thermal hysteresis of the Zerodur material [38] [39] [40].

Changes observed [38] in the thermal expansion of Zerodur (particularly older formulations) can be parts per million depending on annealing parameters. Additionally, it was shown in the same work that there are deviations that are related

to how quickly the Zerodur is thermally cycled. This can account for the regions indicated by the dotted ovals.

The ball/aluminum interface is a sliding contact with inherent friction which can cause forces on all the adhesive joints between the balls and the Zerodur. This is a directional hysteretic effect with the friction force on the balls requiring a balance force (and torque) in the opposite direction and a displacement that is positive with increasing temperature. Using an online calculator [41], the ball/aluminum interfaces were determined to have a Hertzian contact deformation of at most 0.8 micrometers at a normal force of 3 Newtons. This deformation region moves with the ball motion. The friction force was reduced by applying Teflon and graphite (via spray) between the ball/aluminum contact, and neither surface treatment resulted in a substantial effect on the hysteresis with multiple experiment replications.

For substantial swings of humidity, Harmsen [37] determined that there could be as much as 400 nm change in water layer thickness on the surface of a capacitance gauge. There was a demonstrated nonlinear relationship between humidity and water layer thickness observed with a significant time constant involved in the changing thickness of the adsorbed water. Although the work was carried out at various temperatures, changes in water layer thickness as a function of temperature were not reported. However, in the present study, to obtain an optical path difference of 1.4 μm, the total water layer thickness would need to be 1.4 μm divided by the water-air difference in index of refraction (0.333) or 4.2 μm. For the system described in this report, there are eight surfaces in the optical path: two faces on each of the quarter-

wave plates and the polarization beam splitter and one surface for each mirror. This reduces the effect needed to accommodate a 1.4 μm total hysteresis to be near 500 nm per surface (4.2 μm /8). Due to the large surface water layer thickness required, as well as having a hysteretic effect rather than having a temperature dependence, this effect was not thought to be the culprit. However, since the current experimentation varies temperature instead of humidity, estimations of the expected effect here may not be directly possible with reference to the Harmsen [37] work. Additionally, attempts to correlate measured relative humidity and the partial pressure of water in the ambient to the observed spatial variations found no apparent relationships.

Due to a light-weighting web structure on the underside (described in [32]) of the aluminum plate with the vee-grooved top, simple plate bending calculations for plate bowing were not appropriate. But, by plotting the bottom-top difference in temperature of the plate temperature ΔT_{plate} (see Figure 10) to observe similarities, it was observed that the changes and time constants were not consistent with measurement variations. Also plotted in Figure 10 is the temperature difference between the interferometer and the top of the aluminum plate $\Delta T_{int.tp}$. There appears to be a definite similarity in the non-equilibrium features in Figure 9. The mirror displacement was then corrected according to this with a 1 μm/^{0}C (best fit scenario) conversion. The results are plotted in Figure 11.. This does not mean the effect was related to that temperature gradient across that component, but perhaps there is a component with a similar time constant relationship. Consideration was given to whether a gradient in the air temperature and resultant index compensation for the interferometer upper and lower paths was the cause but the compensation would

only produce about 90 nm/^{0}C gradient which is not enough. Similarly, the optics expansion and index thermal changes predicts a coefficient around 250 nm/^{0}C gradient but in the direction that increases the amplitude of the features in question.

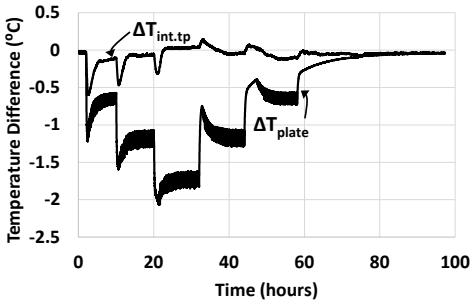

Figure 10. Temperatures differences between the plate top and bottom ΔT_{plate} and between the interferometer and the plate top $\Delta T_{int.tp}$.

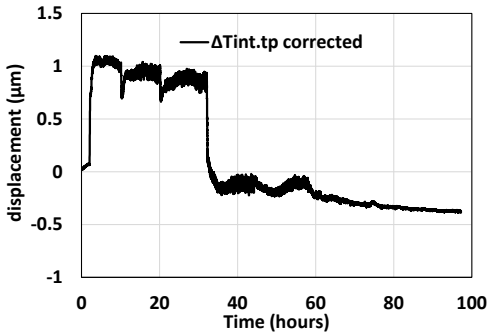

Figure 11. Displacement of the mirrors corrected for the temperature difference between the interferometer and top of the plate. The arbitrary conversion factor was one micrometer per one ^{o}C of optics/plate temperature gradient.

The graph in Figure 11 clearly reveals the hysteresis of the system as the temperature moves from equilibrium to increasing temperature (1 hour mark) and reversing to decreasing temperature (at about 32 hour mark).

Based upon the considerations explored, no absolute causation was determinable as to the actual culprit in the hysteresis and transients in the measurement data.

Finally, the degree that expansion between the mirrors adequately reflects the thermal expansion coefficient of the Zerodur (as the mimicked component of the bowtie structure) was explored. This is considered by plotting the corrected mirror displacement as a function of plate temperature in Figure 12. Using only the cooling data outside the hysteretic region which has a slower thermal transition, the calculated thermal expansion results, 0.11 $\mu/^0$C, are near the expectation values for that of class 2 Zerodur, 0.1 $\mu/^0$C. While the temperature is increasing (non-equilibrium, non-isothermal, fast transition) the full range trend is similar but with significant deviations outside of the expected expansion.

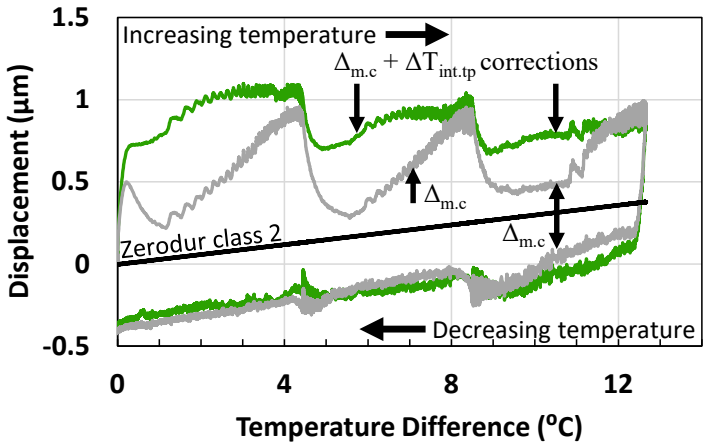

Figure 12. Mirror displacement vs temperature plot after corrections. Also plotted is the theoretical displacement for the thermal expansion of class 2 Zerodur using a length of 305 mm (distance between far spheres).

6. Uncertainty considerations

The uncertainties can be estimated using equation (8) that corrects the mirror displacement laser readings $\Delta m.r$ for each of the previously described factors to obtain the corrected mirror displacement $\Delta m.c$.

$$\Delta_{m.c} = \Delta_{m.r} + \Delta_{air} + \Delta_{op} = \Delta_{m.r} + \Delta_{dTi} + \Delta_{dpi} + \Delta_{dhi} - \Delta_{opl.n.op} - \Delta_{exp.op} \tag{8}$$

Based on the equations used for correction this is expanded and rewritten to equation (9) with common subcomponents and to combine the common (correlated) factors.

$$\begin{aligned}\Delta_{m.c} &= \Delta_{m.r} + l_{air}\, k_T \Delta_T - l_{air}\, k_p \Delta_p + l_{air}\, k_h \Delta_v - l_{op} k_{n.op} \Delta T_{op} - D_{\alpha.op} \Delta T_{op} \\ &= \Delta_{m.r} + l_{air}\left(k_T \Delta_T - k_p \Delta_p + k_h \Delta_v\right) - l_{op}\left(k_{n.op} + k_{\alpha.op}\right)\Delta T_{op}\end{aligned} \tag{9}$$

The uncertainty effects are summarized in Table 1. The thermistors used to sense the various temperatures were calibrated and corrected to a calibrated reference platinum resistance thermometer from 18-33 ^{0}C with better than 0.05^{0}C deviations after corrections. The larger uncertainties used for calculations are due to the placements of the sensors. The air was measured about 100 millimeters away from the laser path (symmetric positions) along with a vertical gradient, and the optics sit on the aluminum plate which heats faster (Figure 10). For the constants, the least significant digit reported or 1% was used as the uncertainty to reflect the maximum effect.

The larger contributors to uncertainty are fixed and not a function of increasing temperature so the uncertainty for the terms that were dependent were calculated for their maximum influence knowing that the effects would be secondary. The estimated uncertainty with a coverage factor of 2 is a 366 nm allowing for an uncertainty of the measured coefficient of expansion between the mirrors to have a nominal estimated uncertainty (366 nm / 12.7 ^{0}C) or about 29 nm/^{0}C placing the reported values for class 2 Zerodur within the expanded uncertainty from the measurements.

Table 1. Measurement uncertainty considerations

Contributor	**Uncertainty**	**Uncertainty effect**
$\Delta m.r$, stability, $U_{L..s}$	$U_{L.s}=10^{-7}$	$U_{L.s}\cdot(l_{air}+n_{BK7}\cdot l_{op})$=26 nm
$\Delta m.r$, resolution, $U_{L.r}$	$U_{L.r}$ = 2 nm (5/√12)	$U_{L.r}$ = 2 nm
l_{air} = 187 mm	$U_{l.air}$ = 2 mm	$U_{l.air}\cdot\Delta_{air}/l_{air}$ = 0.011·Δ_{air} < 20 nm (max)
Δ_T (varies)	U_T =0.5 ^{0}C	$U_T\cdot k_T\cdot l_{air}$ = 87 nm
Δ_p (varies)	U_p = 2 torr	$U_p\cdot k_p\cdot l_{air}$ = 134 nm
Δ_v (varies)	U_v = 3 torr	$U_v\cdot k_h\cdot l_{air}$ = 28 nm
l_{op} = 50.8 mm	$U_{l.op}$ = 0.2 mm	$U_{l.op}\cdot(k_{n.op}+k_{\alpha.op})\cdot\Delta T_{op}$ < 12 nm (max)
ΔT_{op} (varies)	U_{Top} = 0.3 ^{0}C	$U_{Top}\cdot l_{op}\cdot(k_{n.op}+k_{\alpha.op})$ = 65 nm
$k_{n.op}$ =1.18 µ/K	$U_{k.n.op}$ = 0.012 µ/K (1%)	$U_{k.n.op}\cdot l_{op}\cdot\Delta T_{op}$ < 8 nm (max)
$k_{\alpha.op}$ = 3.16 µ/K	$U_{k.\alpha.op}$ = 0.032 µ/K (1%)	$U_{k.\alpha.op}\cdot l_{op}\cdot\Delta T_{op}$ < 21 nm (max)
k_T = 0.93 µ/K	U_{kT} = 0.01 µ/K	$U_{kT}\cdot l_{air}\cdot\Delta_T$ < 25 nm (max)
K_p = 0.36 µ/torr	U_{kp} = 0.01 µ/torr	$U_{kp}\cdot l_{air}\cdot\Delta_p$ < 19 nm (max)
k_h = 0.05 µ/torr	U_{kh} =0.01 µ/torr	$U_{kh}\cdot l_{air}\cdot\Delta_v$ < 13 nm (max)
Root sum squares		**183 nm (max) = $U_{1.m.c}$**
k=2 coverage factor		**366 nm (max) = $U_{2.m.c}$**

Although interferometry was used to ascertain the effectiveness of the bowtie configuration, it would not necessarily be selected for incorporation into an actual measurement or physical setup. However, based on the results of the interferometric measurements, the dimensional stability, S,

of this two-mirror configuration separated by a length L (305 mm here) can be stated by Equation (10). The fixed *1.4 μm* stability is due to the observed hysteresis and non-equilibrium effects (undetermined sources). The *0.1 (μL /^oC)T_R* term is due to the coefficient of thermal expansion of the Zerodur mirror with T_R the range of the ambient temperature. The k(183 nm) term is due to the expanded uncertainty of the interferometric measurement having a coverage factor, k. If another sensor is used to determine the location of a third object between the mirrors then the uncertainty of that sensor would need to be incorporated also.

$$S = 1.4\ \mu m\ +\ \frac{0.1\ \mu\ L}{^0C} T_R + k(183\ nm) \tag{10}$$

7. Summary and embodiment discussion

It was shown that the thermal expansion between two distant points on a plate can be mitigated by a thermal mimicking bowtie mounting design of parallel thermally stable cross members. Measurements confirming the mitigation were facilitated by an interferometric system corrected for atmospheric variations and thermally induced index of refraction changes in the optics. Also observed and considered were hysteretic and temporal deviation effects in non-thermally equilibrated states.

There are manifold ways to implement this design construct not physically demonstrated in this work. The angle fixation could be facilitated with linear slideways with bushings or bearings. Also possible is the use of flexures [42] with the unidirectional compliance constraining the angles. In addition to Zerodur (Schott), other material choices for low expansion cross members are carbon fiber [43] [44], Invar, Clearceram (Ohara), ULE glass (Corning), etc. Mirrors or other measurement

references may be appropriately placed on these elements to produce a thermally stable reference surface for measurements. Additionally, the design may be incorporated into in-situ manufacturing reference fiducial design on tight-tolerance manufactured parts whether small as in the microelectronics industry (e.g. interferometric, moiré patterns) or large [7] as in the aerospace industry. Although this study utilizes nearly congruent triangles, congruence or similarity is not necessary to make the structure thermally invariant.

It is also possible to implement this design in a multi-component configuration in which are all related to the same thermal center on the base (independent material) so that they all expand and contract to a common center. This would be the case with multiple mirror segments or diffraction gratings forming a whole optical unit that is interrelated. Three dimensional variations may also be possible.

Similar to the thermal length balancing by material properties in the designs of thermally invariant pendulums for clocks, the mitigation of thermal expansion using mounting materials having much larger CTE's can also be accomplished with a bowtie design having angularly constrained mounts without common thermal centers as is shown in Figure 13.

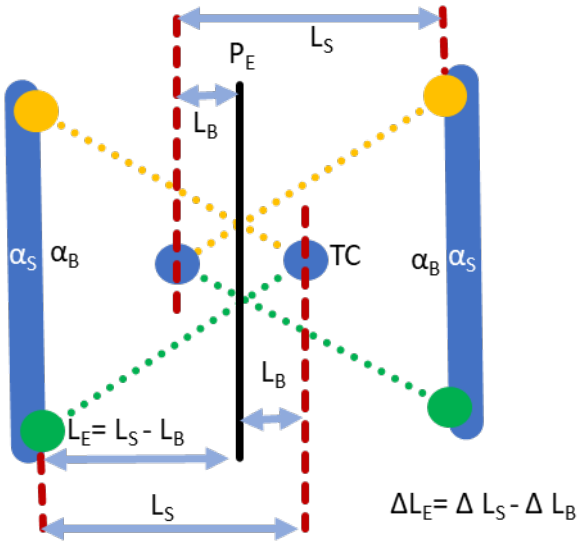

Figure 13. . Overlapping bowtie design, having chosen design lengths, L_S and L_B, so that the effective CTE between the two structurers can be engineered to a nominal preselected value including zero.

In this case the thermal center for the triangle (angularly constrained structure) on the left does not coincide with the thermal center of the triangle on the right. Consider for the moment just the triangle on the left in Figure 13. For a base having a CTE of α_B and a superstructure having a CTE of α_S directly connecting two balls through their centers at a distance L_S from the thermal center. There is a line of equilibrium P_E on the base that can be determined such that there is a nominal zero CTE between it and the superstructure at a distance L_E. Take the distance from the thermal center to P_E to be L_B. From the equation $L_E=L_S-L_B$ then $\Delta L_E=\Delta L_S-\Delta L_B$ where Δ represents the changes in each length. If the effective CTE of the section from PE to the superstructure is α_E, then for a given isothermal temperature change of ΔT for the system, the relationship for the thermal changes in length is given in Equation (11) .

$$\Delta LE = \Delta LS - \Delta LB$$

$$\alpha_E L_E \Delta T = \alpha_S L_S \Delta T - \alpha_B L_B \Delta T$$

$$\alpha_E L_E = \alpha_S L_S - \alpha_B L_B$$

(11)

Setting α_E =0 as the desired effective CTE, the relationship between the lengths L_S and L_B are determined by Equation (12) .

$$0 = \alpha_S L_S - \alpha_B L_B$$

$$\frac{L_S}{L_B} = \frac{\alpha_B}{\alpha_S}$$

(12)

If the equilibrium lines for the left and right triangular structures overlap, both having α_E equal to zero, then the effective CTE between the superstructures is also zero. It is not necessary for the triangular structures to be congruent or similar neither is it necessary for the structures to be made of the same material.

Other embodiments are possible even with negative effective CTE. These embodiments expand the precision engineer's toolbox of design structures for thermal mitigation and mimicry.

Acknowledgements

The following contributed to the material support for this work in some form:

- ORNL, Design and Control of Advanced Machine Tools for Precision Machining
- NASA Phase II SBIR Award 193272, (via sub-contract from Optipro Systems) Advanced nanometer coordinate measuring machine (ANCMM)
- UNC Charlotte Center for Precision Metrology

Neither ORNL, NASA, nor Optipro had any direct involvement in the base research, analysis or writing of this paper.

Thanks to Stuart Smith for proof reading and making suggestions for the improvement of the initial manuscript. Thanks to Geoffrey Heacock for facilitating the final design and machining of the aluminum base plate from simple sketches.

References

[1] Slocum A, Precision Machine Design, Society of Manufacturing Engineers, 1992, p. 96.

[2] Schlamminger S, Chao L, Lee V, Newell DB, Cochrane R and Speake CC, "Beware of Thermal Effects in Precision Measurements," in *Proc Am Soc Precis Eng*, 2023.

[3] Stoop F, Mayr J, Sulz C, Kaftan P, Bleicher F, Yamazaki K and Wegener K, "Cloud-based thermal error compensation with a federated learning approach," *Precis Eng,* vol. 79, pp. 135-145, 2023.

[4] Möhring HC, Wiederkehr P, Erkorkmaz K and Kakinuma Y, "Self-optimizing machining systems," *CIRP Annals Manuf Tech,* vol. 69, no. 2, pp. 740-763, 2020.

[5] "Wikipedia," [Online]. Available: https://en.wikipedia.org/wiki/Pendulum_clock.

[6] Bryan JB, "International Status of Thermal Error research," UCRL, 1967.

[7] Schmitt RH, Peterek M, Morse E, Knapp W, Galetto M, Härtig F, Goch G, Hughes B., Forbes A. and Estler WT, "Advances in Large-Scale Metrology – Review and future trends," *CIRP Annals Manuf Tech,* vol. 65, no. 2, pp. 643-665, 2016.

[8] Bryan JB, McClure ER, Brewer W and Pearson J, "Thermal effects in dimensional metrology," *Mech Eng,* vol. Feb, pp. 26-31, 1966.

[9] Mayr J, Jedrzejewski J, Uhlmann E, Donmez MA, Knapp W, Härtig F, Wendt K, Moriwaki T, Shore P, Schmitt R, Brecher C, Würz T and Wegener K, "Thermal issues in machine tools," *CIRP Ann-Manuf Tech,* vol. 61, no. 2, pp. 771-791, 2012.

[10] Bryan JB, "International Status of Thermal Error Research (1990)," *CIRP Annals,* vol. 39, pp. 645-656, 1990.

[11] Weck M, McKeown P, Bonse R and Herbst U, "Reduction and Compensation of Thermal Errors in Machine Tools," *CIRP Annals Manuf Tech,* vol. 44, no. 2, pp. 589-598, 1995.

[12] Noste T, Hopper L, Miller J and Evans C, "Bearing design choices have consequences: a case study," in *Am Soc Precis Eng Topical Precision spindles and bearings*, Charlotte, 2023.

[13] Huo T, Yu J and Zhao H, "Design of a kinematic flexure mount for precision instruments based on stiffness characteristics of a flexural pivot," *Mechanism and Machine Theory,* vol. 150, no. 103868, 2020.

[14] Sridhar P, Supree S, Bahga SS and Khatait JP, "Design of precision hot embossing machine for micropatterning on PMMA," *ASME. J. Micro Nano-Manuf.,* vol. 9, no. 3, 2021.

[15] Bosman N, Qian JS and Reynaerts D, "Design and experimental validation of an ultra-precision Abbe-compliant linear encoder-based position measurement system," *Precis Eng,* vol. 47, pp. 197-211, 2017.

[16] Bustraan K, "Design principles: a way of working," *Microniek,* 1 2 2010.

[17] Kruis JRCG, Design analysis, testing and applications of two-body and three-body kinematic mounts, Lausanne: EPFL, 2016.

[18] Soemers H, Design Principles for Precision Mechanisms, T-Pointprint, 2011.

[19] Geisen P and Folgering E, "Design guidelines for thermal stability in optomechanical instruments.," *Proc SPIE 5176, Optimechanics,* 2003.

[20] Pijnenburg J, te Voert MJA, de Vreugd J, Vosteen A, van Werkhoven W, Mekking J and Nijland BAH, "Ultra-stable isostatic bonded optical mount design for harsh environments," in *Proc. SPIE 8450, Modern TEchnologies in Space and Ground-based Telescopes and Instrumentation II*, 2012.

[21] Slocum A, "Kinematic couplings: A review of design principles and applications," *IJMTM,* vol. 50, no. 4, pp. 310-327, 2010.

[22] Blanding DL, Exact Constraint: Machine design using kinematic principles, ASME Press, 1999, pp. 21, 90-99.

[23] Wilendorf WH, Fernández PS , Geraldes RR, Kofukuda LM, Neckel IT and Tolentino HCN, "Electrochemistry and Microfluidic Environments for the TARUMÃ Station at the CARNAÚBA Beamline at Sirius/LNLS," in *Proc. MEDSI'20*, Chicago, 2021.

[24] Werner C, Rosielle PCJN and Steinbuch M, , "Design of a long stroke translation stage for AFM," *International Journal of Machine Tools and Manufacture,* vol. 50, no. 2, pp. 183-190, 2010.

[25] Nijenhuis JR and Giesen PTM, "Mechanisms enabling observation of Jupiter like planets in deep space," *Optomechanics,* vol. 5877, p. 587706, 2005.

[26] Zhou X, Zhang Y, Jiang Y, Ding S, Sun L and Yang J, "A horizontal-axis spaceborne primarymirror design," *Optik,* vol. 224, p. 165671, 2020.

[27] Geralde RR, Claudiano GV, Ferre VZ, Sanfelici L, Sikorsk A, Souza MS and Tol HCN, "The design of exacly constrained X-ray mirro systems for Sirius," in *MEDSI2018*, Paris, France, 2018.

[28] Henein S, Spanoudakis P, Schwab P, Kjelberg I, Girlens L, Welte Y, Greger LDR and Langer U, "LISA: Design and development of the point-ahead angle mechanism for the laser interferometer space antenna (LISA)," in *Proc 13th European Space Mechanisms and Tribology Symposium ESMATS*, 2009.

[29] Bosmans N and Reynaerts D, "Force Loops," in *Basics of Precision Engineering*, 2018, p. 505.

[30] Yoder P and Vukobratovich D, Opto-mechanical Systems Design, Two Volumes, CRC Press, 2015, p. 1672.

[31] Phillips J, Freedom in machinery, Vol 1: Introducing screw theory, Cambridge University Press, 1984, p. 19.

[32] Miller J and Heacock G, "Thermal chamber design and optical alignment for testing thermal mitigation using bowtie mounting configuration," in *Proc. Am Soc for Precision Eng Annual Meeting*, Boston, 2023.

[33] ASME, B5.57 Methods for preformance evaluation of computer numerically controlled lathes and turning centers, 1998.

[34] Schott, "TIE-19 Temperature coefficient of the refractive index," July 2016. [Online]. Available: https://www.schott.com/en-us/search?q=TIE-19. [Accessed July 2023].

[35] Schott, "Optical Glass Datasheets," February 2014. [Online]. Available: https://www.schott.com/en-us/products/optical-glass-p1000267/downloads. [Accessed June 2023].

[36] Whitehead TN, The design and use of instruments and accurate mechanism, Dover, 1954.

[37] Harmsen W, The excessive humidity effect on capacitive distance sensors for precision positioning, TU Delft, 2010.

[38] Jacobs S, Johnston S and Hansen G, "Expansion hysteresis upon thermal cycling of Zerodur," *Appl Opt,* vol. 23, pp. 3014-6, 1984.

[39] Pannhorst W, Haug R, Rodek E and Stetter K, "Hysteresis effects in low expansion glass-ceramics," *J Non-Cryst Solids,* Vols. 131-133, pp. 488-491, 1991.

[40] Russell R, "Zerodur," 2011. [Online]. Available: https://wp.optics.arizona.edu/optomech/wp-content/uploads/sites/53/2016/10/Tutorial_Russell-Robert.pdf. [Accessed July 2023].

[41] Precision Mindset, "Hertzian Contact: Sphere against a flat," [Online]. Available: http://www.precisionmindsetllc.com/Calculators/HertzianContact/sphere-against-a-flat.html. [Accessed July 2023].

[42] Smith ST, Flexures: Elements of elastic mechanisms, CRC Press, 2000.

[43] Miller JA, Aguilar JJ, Saad M and Caskey GW, "Interferometric measurement of the low value CTE of a ball bar," in *Proc Am Soc Precis Eng 2010 Annual Meeting*, Atlanta, GA, 2010.

[44] Rockwest Composites, [Online]. Available: https://www.rockwestcomposites.com/45690-zte. [Accessed 28 June 2023].

Figure captions

Figure 1. Trigonometric law of sines illustrated.
Figure 2. Bowtie configuration utilizing symmetric triangles and the law of sines
Figure 3. The physically realized bowtie (dashed lines) configuration photographed from above. Each mirror is held by three balls. The balls are kinematically seated in the radially machined vee-groves of an aluminum plate. The outer balls set the vertices of the nearly symmetric triangles. The inset shows electro-discharge machined slot in mounting ball. The apparent distortion is caused by the camera pose.
Figure 4. Temperature of the top surface of the aluminum baseplate over time. There were three controlled steps in temperature up and down with differing step durations accounting for the different time constants for heating and cooling.
Figure 5. Schematic of the components and beam paths for the mirrors' displacement measurements. The components, beam paths and polarizations are identified. The paths in the PBS optical element are unbalanced. The actual paths setup is over/under and not side-to-side.
Figure 6. Nominal and interferometric indications between mirrors mounted on an aluminum plate in response to a stepped thermal environment, are plotted. The left axis indicates the base expansion and the right axis the interferometric indications before and after correction for wavelength refraction factors explained in the text.
Figure 7. Corrections to the measurements for the changing index of refraction of air due to temperature, humidity, and pressure.
Figure 8, The corrections made for the thermally changing index of refraction affecting the optical path length through the interferometer optics.
Figure 9. Displacement between mirrors after correction for the changing index of air and optics. The circled regions are thermal non-equilibrium regions of interest described further in the text.
Figure 10. Temperatures differences between the plate top and bottom ΔT_{plate} and between the interferometer and the plate top $\Delta T_{int.tp}$.
Figure 11. Displacement of the mirrors corrected for the temperature difference between the interferometer and top of the plate. The arbitrary conversion factor was one micrometer per one ^{o}C of optics/plate temperature gradient.
Figure 12. Mirror displacement vs temperature plot after corrections. Also plotted is the theoretical displacement for the thermal expansion of class 2 Zerodur using a length of 305 mm (distance between far spheres).

Figure 13. . Overlapping bowtie design, having chosen design lengths, L_S and L_B, so that the effective CTE between the two structurers can be engineered to a nominal preselected value including zero.

Nomenclature

Symbol	Description
TC	thermal center
a, b. c a', b' c'	vertices of a triangle
A, B, C A', B', C'	sides of a triangle
α, β, γ α', β', γ'	angles of a triangles opposite sides A, B, C and A'. B' C'
PBS	polarization beam splitter
QWP	quarter wave plate
RR	retroreflector
M	mirror
$m.r$	interferometer measurement readings
m.c	corrected interferometer readings
l_{air}	physical path length in air
d_{qwp}	physical laser path length through QWPs
d_{pbs}	unbalanced physical laser path through PBS
$\Delta m.r$	change in *m.r*
$\Delta m.c$	change in *m.c*
Δ_{dTi}	change in optical path length in air due to temperature change Δ_T
Δ_{dpi}	change in optical path length in air due to pressure change Δp
Δ_{dhi}	change in optical path length in air due to Δv (humidity, Δ_T effect)
Δ_{air}	correction for optical path length in air due to T, P, and H
k_T	change in Δ_{air} per unit Δ_T per unit length of path
K_p	change in Δ_{air} per unit Δp per unit length of path
k_h	change in Δ_{air} per unit Δv per unit length of path
Δ_T	change in temperature of air path
Δp	change in pressure of air path
Δv	change in partial pressure H_2O in air path
l_{op}	unbalanced optical physical path length through optics
ΔT_{op}	change in temperature of optical element
Δ_{op}	correction of optical path length through optics
$D_{n.op}$	change in optical path length per temperature change due to $n(\Delta T_{op})$
$n(\Delta T_{op})$	index of refraction as a function of ΔT_{op}
$k_{n.op}$	$D_{n.op}$ per unit length of BK7 glass
$D_{\alpha.op}$	change in optical path length due to optics expansion
$k_{\alpha.op}$	change in optical path per unit length due to optics expansion

α_{BK7}	thermal expansion coefficient of BK7
BK7	an optical glass type
n_{BK7}	index of refraction of BK7
n_{air}	index of refraction of air
$\Delta_{n.op}$	change in n_{BK7} due to ΔT_{op}
$\Delta_{opl.n.op}$	change in optical path due to $\Delta_{n.op}$
$\Delta_{exp.op}$	change in optical path due to thermal expansion of optics
Δ_{op}	Total change in optical path through optics ($\Delta_{exp.op}$, $\Delta_{opl.n.op}$)
ΔT_{plate}	change in temperature of plate top
$\Delta T_{int.tp}$	temperature difference between optics and plate
$U_{L.s}$	laser stability uncertainty
$U_{L.r}$	uncertainty due to interferometer resolution
$U_{l.air}$	uncertainty of air path length
U_T	uncertainty of air temperature
U_p	uncertainty of air pressure
U_v	uncertainty of partial pressure of H_2O in air
$U_{l.op}$	uncertainty of unbalanced physical path through optics
U_{Top}	uncertainty of optics temperature
$U_{k.n.op}$	uncertainty of optics path length index correction constant
$U_{k.\alpha.op}$	uncertainty of optics expansion correction constant
U_{kT}	uncertainty of air temperature correction constant
U_{kp}	uncertainty of air pressure correction constant
U_{kh}	uncertainty of air humidity correction constant
$U_{1.m.c}$	corrected measurement uncertainty, coverage factor of 1
$U_{2.m.c}$	corrected measurement uncertainty, coverage factor of 2
P_E	line of equilibrium (thermal)
L_S	length from kinematic superstructure to TC
L_B	length from PE to TC
L_E	length from PE to kinematic superstructure
ΔL_S	change in length of L_S
ΔL_B	change in length of L_B
ΔL_E	change in length of L_E
α_S	CTE of kinematic superstructure
α_B	CTE of kinematic base
α_E	effective CTE from P_E to kinematic superstructure